Article

Localization of Small Objectives from Scattering Parameter via Bistatic Measurement Configuration

Seong-Ho Son [1] **and Won-Kwang Park** [2,*]

1   Department of Mechanical Engineering, Soonchunhyang University, Asan 31538, Korea
2   Department of Information Security, Cryptology and Mathematics, Kookmin University, Seoul 02707, Korea
*   Correspondence: parkwk@kookmin.ac.kr

Abstract: We develop a sampling-type algorithm for localizing a small object from scattering parameter data measured in a bistatic configuration. To this end, we design a sampling-type imaging function based on the integral equation formula for the scattering parameter. To clarify its applicability, we show that the imaging function can be expressed by the bistatic angle, antenna arrangement, and Bessel function of an integer order. This result reveals some properties of the imaging function and influence of the selection of the bistatic angle. Numerical experiments are carried out for single and multiple small and large objectives to illustrate the pros and cons of the developed algorithm.

Keywords: Bessel function; bistatic imaging; scattering parameter; simulation results

1. Introduction

There are a number of interesting and notable microwave imaging (MI) technologies that have important applications, such as tomography imaging [1,2], breast imaging [3,4], crack detection in nondestructive testing [5,6], thermal therapy monitoring [7], and stroke diagnosis [8,9] that are highly related to human life.

Typically, the purpose of MI is to determine the parameter distribution of a region of interest from measured scattering parameter data. The difficulty of this problem arises from its intrinsic nonlinearity and ill-posedness. To alleviate this challenge, various nonlinear inversion techniques, most of which are iteration schemes, have been developed. For example, the Gauss–Newton inversion [10,11], Born iterative method [12,13], Levenberg–Marquardt algorithm [14,15], contrast source inversion method [16,17], and level set method [18,19]. For a successful application of these schemes, one needs a good initial guess and a proper selection of regularization.

Alternatively, various non-iterative schemes have been designed and successfully applied to MI, such as multiple signal classification (MUSIC) [20,21], migration techniques [22,23], direct and orthogonality sampling methods [24,25], and the factorization method [3,26]. Most of these techniques are developed under the multistatic measurement system (MMS). However, it is not convenient to apply MMS-based schemes in certain applications, such as ground penetrating radar (GPT). Recently, as an alternative, various imaging techniques in the monostatic measurement configuration have been investigated; refer to [27–29]. However, in some problems, it is difficult to measure the scattering parameter data when the transmitter and receiver are in the same position and to discern the weak scattered signal from the relatively high antenna reflection (see [30,31] for instance). Thus, it is natural to consider the development of an imaging technique in which the positions of the transmitter and receiver are different.

Bistatic radar is a radar system consisting of spatially separated single transmitting and receiving antennas [32] and bistatic imaging is a radar imaging technique using bistatic radar. Thus, it does not belong to MMS and is very useful in several practical applications, such as biomedical imaging for breast cancer detection [33], microwave imaging [34],

synthetic aperture radar [35], upper atmospheric studies [36], and cylindrical millimeter-wave imaging for concave objects [37]. We also mention [38–41] as valuable references that contain the basic concept of bistatic radar and imaging technique and its application to various problems. However, little has been developed for designing an effective non-iterative scheme and investigating reliable mathematical theories to explain its applicability and fundamental limitation. Therefore, the impetus of this research is to design a sampling-type algorithm for imaging small objects and establish a mathematical theory.

This paper is constructed as follows. In Section 2, the notion of the scattering parameter is introduced, a bistatic measurement configuration is illustrated, and the sampling-type imaging algorithm is sketched. In Section 3, we establish a mathematical theory to demonstrate that the localization of objective is dependent on the total number of measurement data, antenna arrangement, and bistatic angle. In Section 4, numerical results are shown to demonstrate the pros and cons of the designed algorithm. Section 5 contains a short conclusion and perspectives.

2. Overview of Scattering Parameter and Design of Imaging Function

Assume that a small objective Σ is located in a two-dimensional homogeneous region. For the sake, we set Σ as a circle of radius α with location $\mathbf{r}_{\mathrm{obj}}$ and is enclosed by N antennas to transmit and receive signals with location $\mathbf{a}_m$, $m = 1, 2, \cdots, M$, on a circle of radius R. Let $\Omega \subset \mathbb{R}^2$ be the region of interest (ROI) such that $\mathbf{a}_m$ is located at the exterior of Ω.

In this study, every material is characterized by its permittivity and conductivity at a given angular frequency $\omega = 2\pi f$. So, for every $\mathbf{r} \in \Omega$, we set the permeability as a constant $\mu(\mathbf{r}) = \mu_{\mathrm{b}}$. We denote $\varepsilon_{\mathrm{obj}}$ and ε_{b} as the permittivity of Σ and Ω, respectively, and assume that $\varepsilon_{\mathrm{b}} \gg \sigma_{\mathrm{b}}/\omega$. Furthermore, the conductivities σ_{obj} and σ_{b} can be defined analogously. With this, we define the following piecewise permittivity and conductivity as $\varepsilon(\mathbf{r})$ and $\sigma(\mathbf{r})$, respectively, such that

$$\varepsilon(\mathbf{r}) = \begin{cases} \varepsilon_{\mathrm{obj}} & \text{for} \quad \mathbf{r} \in \Sigma, \\ \varepsilon_{\mathrm{b}} & \text{for} \quad \mathbf{r} \in \Omega \backslash \Sigma, \end{cases} \quad \text{and} \quad \sigma(\mathbf{r}) = \begin{cases} \sigma_{\mathrm{obj}} & \text{for} \quad \mathbf{r} \in \Sigma, \\ \sigma_{\mathrm{b}} & \text{for} \quad \mathbf{r} \in \Omega \backslash \Sigma, \end{cases}$$

With this, we introduce the background wavenumber k that satisfies $k^2 = \omega^2 \mu_{\mathrm{b}} \varepsilon_{\mathrm{b}} + i\omega\mu_{\mathrm{b}}\sigma_{\mathrm{b}}$.

Let $\Delta S(m', m)$ be the scattered field S-parameter introduced in [7] that is given by

$$\Delta S(m', m) = \frac{ik^2}{4\omega\mu_{\mathrm{b}}} \int_{\Omega} \left(\frac{\varepsilon(\mathbf{r}) - \varepsilon_{\mathrm{b}}}{\varepsilon_{\mathrm{b}}} + i\frac{\sigma(\mathbf{r}) - \sigma_{\mathrm{b}}}{\omega\varepsilon_{\mathrm{b}}} \right) \mathrm{E}_{\mathrm{inc}}(\mathbf{a}_m, \mathbf{r}) \mathrm{E}_{\mathrm{tot}}(\mathbf{r}, \mathbf{a}_{m'}) d\mathbf{r}, \tag{1}$$

where $\mathrm{E}_{\mathrm{inc}}(\mathbf{a}_m, \mathbf{r})$ and $\mathrm{E}_{\mathrm{tot}}(\mathbf{r}, \mathbf{a}_{m'})$ are the z-component of the incident field $\mathbf{E}_{\mathrm{inc}}(\mathbf{a}_m, \mathbf{r})$ and the total field $\mathbf{E}_{\mathrm{tot}}(\mathbf{r}, \mathbf{a}_n)$, respectively. Notice that from the Maxwell equation, $\mathbf{E}_{\mathrm{inc}}(\mathbf{a}_m, \mathbf{r})$ and $\mathbf{E}_{\mathrm{tot}}(\mathbf{r}, \mathbf{a}_n)$ satisfy

$$\nabla \times \mathbf{E}_{\mathrm{inc}}(\mathbf{a}_m, \mathbf{r}) = -i\omega\mu_{\mathrm{b}}\mathbf{H}_{\mathrm{tot}}(\mathbf{a}_m, \mathbf{r}) \quad \text{and} \quad \nabla \times \mathbf{H}_{\mathrm{inc}}(\mathbf{a}_m, \mathbf{r}) = (\sigma_{\mathrm{b}} + i\omega\varepsilon_{\mathrm{b}})\mathbf{E}_{\mathrm{inc}}(\mathbf{a}_m, \mathbf{r}),$$

and

$$\nabla \times \mathbf{E}_{\mathrm{tot}}(\mathbf{r}, \mathbf{a}_{m'}) = -i\omega\mu_{\mathrm{b}}\mathbf{H}_{\mathrm{tot}}(\mathbf{r}, \mathbf{a}_{m'}) \quad \text{and} \quad \nabla \times \mathbf{H}_{\mathrm{tot}}(\mathbf{r}, \mathbf{a}_{m'}) = (\sigma(\mathbf{r}) + i\omega\varepsilon(\mathbf{r}))\mathbf{E}_{\mathrm{tot}}(\mathbf{r}, \mathbf{a}_{m'}),$$

respectively. Here, we assume a time-harmonic dependence $e^{i\omega t}$, and $\mathbf{H}$ denotes the magnetic field.

Unfortunately, we cannot design an imaging function because the closed form of the $\mathrm{E}_{\mathrm{tot}}$ in (1) is still unknown. Notice that to use the closed form, one must know complete information of Σ. Instead, we assume that the value of α satisfies

$$\left(\sqrt{\frac{\varepsilon_{\mathrm{obj}}}{\varepsilon_{\mathrm{b}}}} - 1 \right) \alpha < \frac{\lambda}{4}.$$

Then, applying Born approximation (see based on [42]) and reciprocity property of the incident field, we can obtain the following approximation for $\Delta S(m', m)$

$$\Delta S(m', m) \approx \frac{ik^2\alpha^2\pi}{4\omega\mu_{\rm b}} \left(\frac{\varepsilon_{\rm obj} - \varepsilon_{\rm b}}{\varepsilon_{\rm b}} + i\frac{\sigma_{\rm obj} - \sigma_{\rm b}}{\omega\varepsilon_{\rm b}} \right) {\rm E}_{\rm inc}(\mathbf{a}_m, \mathbf{r}_{\rm obj}) {\rm E}_{\rm inc}(\mathbf{a}_{m'}, \mathbf{r}_{\rm obj}). \tag{2}$$

Now, let us design a sampling-type imaging function. For this, let us consider the following arrangement of M-different measurement data:

$$\mathbf{V}_{\rm meas}^{(n)} = \Big(\Delta S(\psi_1, 1), \Delta S(\psi_2, 2), \cdots, \Delta S(\psi_M, M) \Big),$$

where $\psi_m = m' = (m + n - 1 \pmod{M}) + 1$, $\mathbf{a}_m = R(\cos\theta_m, \sin\theta_m)$, $\mathbf{a}_{m'} = R(\cos\theta_{m'}, \sin\theta_{m'})$, and $\theta_{m'} = \theta_m + \beta$. Here, β denotes the bistatic angle; refer to Figure 1 for an illustration.
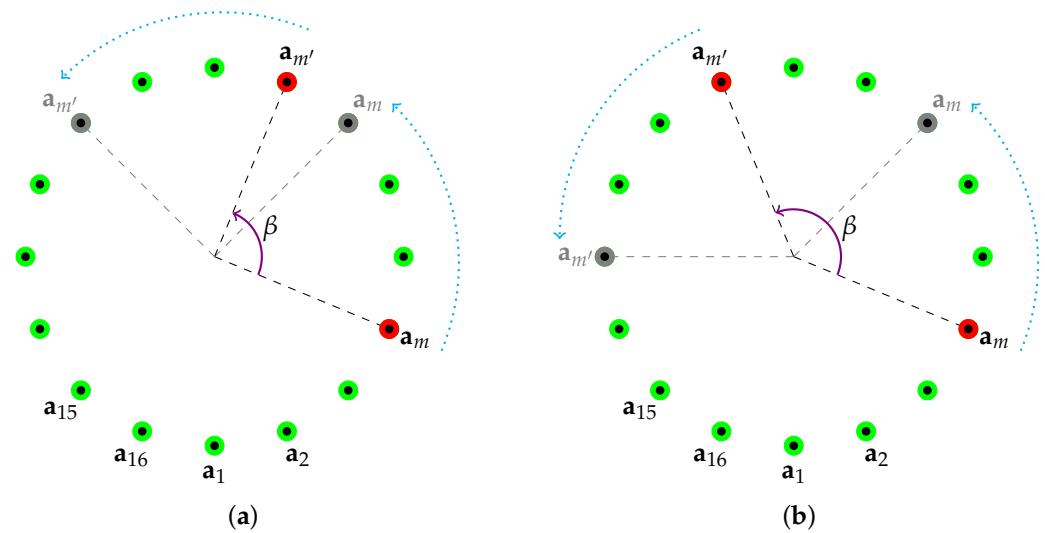

Figure 1. Illustration of bistatic measurement configuration. (**a**) $n = 4$ case, (**b**) $n = 6$ case.

Based on the structure of $\Delta S(m', m)$ of (2), the arrangement $\mathbf{V}_{\rm meas}^{(n)}$ can be written as

$$\mathbf{V}_{\rm meas}^{(n)} \approx \frac{ik^2\alpha^2\pi}{4\omega\mu_{\rm b}} \left(\frac{\varepsilon_{\rm obj} - \varepsilon_{\rm b}}{\varepsilon_{\rm b}} + i\frac{\sigma_{\rm obj} - \sigma_{\rm b}}{\omega\varepsilon_{\rm b}} \right) \Big({\rm E}_{\rm inc}(\mathbf{a}_1, \mathbf{r}_{\rm obj}) {\rm E}_{\rm inc}(\mathbf{a}_{\psi_1}, \mathbf{r}_{\rm obj}),$$

$${\rm E}_{\rm inc}(\mathbf{a}_2, \mathbf{r}_{\rm obj}) {\rm E}_{\rm inc}(\mathbf{a}_{\psi_2}, \mathbf{r}_{\rm obj}), \cdots, {\rm E}_{\rm inc}(\mathbf{a}_M, \mathbf{r}_{\rm obj}) {\rm E}_{\rm inc}(\mathbf{a}_{\psi_M}, \mathbf{r}_{\rm obj}) \Big).$$

Based on this observation, we test the orthogonality relation between $\Delta S(m', m)$ and ${\rm E}_{\rm inc}(\mathbf{a}_m, \mathbf{r}_{\rm obj}) {\rm E}_{\rm inc}(\mathbf{a}_{m'}, \mathbf{r}_{\rm obj})$ on the Hilbert space ℓ^2 to extract $\mathbf{r}_{\rm obj}$ from the arrangement $\mathbf{V}_{\rm meas}^{(n)}$. To this end, we introduce the following vector for $\mathbf{r} \in \Omega$,

$$\mathbf{V}_{\rm test}(\mathbf{r}) = \Big({\rm E}_{\rm inc}(\mathbf{a}_1, \mathbf{r}) {\rm E}_{\rm inc}(\mathbf{a}_{\psi_1}, \mathbf{r}), {\rm E}_{\rm inc}(\mathbf{a}_2, \mathbf{r}) {\rm E}_{\rm inc}(\mathbf{a}_{\psi_2}, \mathbf{r}), \cdots, {\rm E}_{\rm inc}(\mathbf{a}_M, \mathbf{r}) {\rm E}_{\rm inc}(\mathbf{a}_{\psi_M}, \mathbf{r}) \Big).$$

Then, based on the property of inner (or dot) product on ℓ^2-space, we can examine that

$$\left| \left\langle \frac{\mathbf{V}_{\rm meas}^{(n)}}{|\mathbf{V}_{\rm meas}^{(n)}|}, \frac{\mathbf{V}_{\rm test}(\mathbf{r})}{|\mathbf{V}_{\rm test}(\mathbf{r})|} \right\rangle_{\ell^2} \right| = \begin{cases} 1 & \text{if} \quad \mathbf{r} = \mathbf{r}_{\rm obj} \\ \text{between 0 and 1} & \text{if} \quad \mathbf{r} \neq \mathbf{r}_{\rm obj}, \end{cases}$$

where the inner product $\langle \cdot, \cdot \rangle_{\ell^2}$ is defined as $\langle \mathbf{A}, \mathbf{B} \rangle_{\ell^2} = \mathbf{A} \cdot \overline{\mathbf{B}}$.

Based on this observation, the following imaging function can be introduced:

$$\mathfrak{F}_{\text{BS}}(\mathbf{r}, n) = \frac{|\mathbf{V}_{\text{meas}}^{(n)} \cdot \overline{\mathbf{V}_{\text{test}}(\mathbf{r})}|}{\|\mathbf{V}_{\text{meas}}^{(n)}\| \|\mathbf{V}_{\text{test}}(\mathbf{r})\|} = \frac{|\Phi(\mathbf{r})|}{\max\limits_{\mathbf{r} \in \Omega} |\Phi(\mathbf{r})|}, \tag{3}$$

where

$$\Phi(\mathbf{r}) = \sum_{m=1}^{M} \Delta S(m', m) \overline{\mathbf{E}_{\text{inc}}(\mathbf{a}_m, \mathbf{r}) \mathbf{E}_{\text{inc}}(\mathbf{a}_{m'}, \mathbf{r})}.$$

Then, $\mathfrak{F}_{\text{BS}}(\mathbf{r}, n) \approx 1$ when $\mathbf{r} \approx \mathbf{r}_{\text{obj}} \in \Sigma$ and $0 \leq \mathfrak{F}_{\text{BS}}(\mathbf{r}, n) < 1$ when $\mathbf{r} \notin \Sigma$. Therefore, it is possible to identify $\mathbf{r}_{\text{obj}}$ through the map of $\mathfrak{F}_{\text{BS}}(\mathbf{r}, n)$.

3. Analysis of Imaging Function and Some Properties

Based on the designed imaging function (3) in the previous Section, we expect to successfully identify an objective. However, the identification performance is significantly dependent on the bistatic angle or equivalently n. To explain such a phenomenon and select an optimal value n, we establish a reliable mathematical theory for the imaging function. To this end, we derive the following result.

Theorem 1. *Let* $\mathbf{r}_{\text{obj}} - \mathbf{r} = |\mathbf{r}_{\text{obj}} - \mathbf{r}|(\cos\phi_{\text{obj}}, \sin\phi_{\text{obj}})$, $\boldsymbol{\theta}_m = \mathbf{a}_m/|\mathbf{a}_m| = (\cos\theta_m, \sin\theta_m)$, *and* $\theta_{m'} = \theta_m + \beta$. *Then for each* $\mathbf{r} \in \Omega$ *that satisfies* $|\mathbf{a}_m - \mathbf{r}| \gg (4|k|)^{-1}$, $m = 1, 2, \cdots, M$, $\mathfrak{F}_{\text{BS}}(\mathbf{r}, n)$ *can be represented as follows:*

$$\mathfrak{F}_{\text{BS}}(\mathbf{r}, n) = \frac{|\Psi(\mathbf{r})|}{\max\limits_{\mathbf{r} \in \Omega} |\Psi(\mathbf{r})|}, \tag{4}$$

where

$$\Psi(\mathbf{r}) = J_0(k(1 + \cos\beta)|\mathbf{r}_{\text{obj}} - \mathbf{r}|) J_0(k\sin\beta|\mathbf{r}_{\text{obj}} - \mathbf{r}|)$$
$$+ \frac{1}{M} \sum_{m=1}^{M} \Big((\Lambda_2 + \Lambda_3) J_0(k(1 + \cos\beta)|\mathbf{r}_{\text{obj}} - \mathbf{r}|) + \Lambda_1 J_0(k\sin\beta|\mathbf{r}_{\text{obj}} - \mathbf{r}|) + \Lambda_1(\Lambda_2 + \Lambda_3) \Big).$$

Here, J_s *denotes the Bessel function of order s and*

$$\Lambda_1 = 2 \sum_{s=1}^{\infty} i^s J_s(k(1 + \cos\beta)|\mathbf{r}_{\text{obj}} - \mathbf{r}|) \cos\big(s(\theta_m - \phi_{\text{obj}})\big),$$

$$\Lambda_2 = 2 \sum_{s=1}^{\infty} J_{2s}(k\sin\beta|\mathbf{r}_{\text{obj}} - \mathbf{r}|) \cos\big(2s(\theta_m - \phi_{\text{obj}})\big),$$

$$\Lambda_3 = -2i \sum_{s=0}^{\infty} J_{2s+1}(k\sin\beta|\mathbf{r}_{\text{obj}} - \mathbf{r}|) \sin\big((2s + 1)(\theta_m - \phi_{\text{obj}})\big).$$

Proof. Since $|\mathbf{a}_m - \mathbf{r}| \gg (4|k|)^{-1}$ for $m = 1, 2, \cdots, M$, we can examine that (see [43] for instance)

$$\mathbf{E}_{\text{inc}}(\mathbf{a}_m, \mathbf{r}) = \frac{i}{4} H_0^{(2)}(k|\mathbf{a}_m - \mathbf{r}|) \approx \frac{(-1 + i)e^{-ikR}}{4\sqrt{k\pi R}} e^{ik\boldsymbol{\theta}_m \cdot \mathbf{r}}.$$

Then, $\Phi(\mathbf{r})$ defined in (3) becomes

$$\Phi(\mathbf{r}) = \sum_{m=1}^{M} \Delta S(m', m) \overline{\mathbf{E}_{\text{inc}}(\mathbf{a}_m, \mathbf{r}) \mathbf{E}_{\text{inc}}(\mathbf{a}_{m'}, \mathbf{r})} = \frac{i\alpha^2 \mathcal{O}(\mathbf{r}_{\text{obj}})}{256\pi R^2} \sum_{m=1}^{M} e^{ik\boldsymbol{\theta}_m \cdot (\mathbf{r}_{\text{obj}} - \mathbf{r})} e^{ik\boldsymbol{\theta}_{m'} \cdot (\mathbf{r}_{\text{obj}} - \mathbf{r})}.$$

Since $\theta_{m'} = \theta_m + \beta$, we have

$$
\begin{aligned}
(\cos\theta_m &+ \cos(\theta_m + \beta), \sin\theta_m + \sin(\theta_m + \beta)) \cdot (\cos\phi_{\text{obj}}, \sin\phi_{\text{obj}}) \\
&= (\cos\theta_m + \cos\theta_m \cos\beta - \sin\theta_m \sin\beta, \sin\theta_m + \sin\theta_m \cos\beta + \cos\theta_m \sin\beta) \\
&\quad \cdot (\cos\phi_{\text{obj}}, \sin\phi_{\text{obj}}) \\
&= (1 + \cos\beta)\cos\theta_m \cos\phi_{\text{obj}} - \sin\beta \sin\theta_m \cos\xi + (1 + \cos\beta)\sin\theta_m \sin\phi_{\text{obj}} \\
&\quad + \sin\beta \cos\theta_m \sin\phi_{\text{obj}} \\
&= (1 + \cos\beta)\cos(\theta_m - \phi_{\text{obj}}) - \sin\beta \sin(\theta_m - \phi_{\text{obj}})
\end{aligned}
$$

and correspondingly,

$$
(\boldsymbol{\theta}_m + \boldsymbol{\theta}_{m'}) \cdot (\mathbf{r}_{\text{obj}} - \mathbf{r}) = |\mathbf{r}_{\text{obj}} - \mathbf{r}|\big((1 + \cos\beta)\cos(\theta_m - \phi_{\text{obj}}) - \sin\beta \sin(\theta_m - \phi_{\text{obj}})\big).
$$

Thus, $\Phi(\mathbf{r})$ becomes

$$
\Phi(\mathbf{r}) = \frac{i\alpha^2 \mathcal{O}(\mathbf{r}_{\text{obj}})}{256\pi R^2} \sum_{m=1}^{M} e^{ik|\mathbf{r}_{\text{obj}} - \mathbf{r}|[(1+\cos\beta)\cos(\theta_m - \phi_{\text{obj}}) - \sin\beta \sin(\theta_m - \phi_{\text{obj}})]}. \tag{5}
$$

Now, let us recall the following Jacobianger expansion formulas:

$$
\begin{aligned}
e^{ix\cos\theta} &= J_0(x) + 2\sum_{s=1}^{\infty} i^s J_s(x)\cos(s\theta), \\
e^{-ix\sin\theta} &= J_0(x) + 2\sum_{s=1}^{\infty} J_{2s}(x)\cos(2s\theta) - 2i\sum_{s=0}^{\infty} J_{2s+1}(x)\sin\big((2s+1)\theta\big).
\end{aligned} \tag{6}
$$

Then, since

$$
\begin{aligned}
e^{ik|\mathbf{r}_{\text{obj}} - \mathbf{r}|(1+\cos\beta)\cos(\theta_m - \phi_{\text{obj}})} &= J_0(k(1+\cos\beta)|\mathbf{r}_{\text{obj}} - \mathbf{r}|) \\
&\quad + 2\sum_{s=1}^{\infty} i^s J_s(k(1+\cos\beta)|\mathbf{r}_{\text{obj}} - \mathbf{r}|)\cos\big(s(\theta_m - \phi_{\text{obj}})\big)
\end{aligned} \tag{7}
$$

and

$$
\begin{aligned}
e^{-ik|\mathbf{r}_{\text{obj}} - \mathbf{r}|\sin\beta \sin(\theta_m - \phi_{\text{obj}})} &= J_0(k\sin\beta|\mathbf{r}_{\text{obj}} - \mathbf{r}|) \\
&\quad + 2\sum_{s=1}^{\infty} J_{2s}(k\sin\beta|\mathbf{r}_{\text{obj}} - \mathbf{r}|)\cos\big(2s(\theta_m - \phi_{\text{obj}})\big) \\
&\quad - 2i\sum_{s=0}^{\infty} J_{2s+1}(k\sin\beta|\mathbf{r}_{\text{obj}} - \mathbf{r}|)\sin\big((2s+1)(\theta_m - \phi_{\text{obj}})\big),
\end{aligned} \tag{8}
$$

we can immediately obtain structure (4) by plugging (7) and (8) into (5).　□

Based on the Theorem 1, we can explore some properties of the $\mathfrak{F}_{\text{BS}}(\mathbf{r}, n)$.

Property 1 (Role of the factors). *Since $J_0(0) = 1$ and $J_s(0) = 0$ for $s = 1, 2, \cdots$, the terms $J_0(k(1+\cos\beta)|\mathbf{r}_{\text{obj}} - \mathbf{r}|)$ and $J_0(k\sin\beta|\mathbf{r}_{\text{obj}} - \mathbf{r}|)$ contribute to identifying the objective location. On the other side, since the terms Λ_l, $l = 1, 2, 3$ satisfy*

$$
\lim_{\mathbf{r} \to \mathbf{r}_{\text{obj}}} \Lambda_l = 0,
$$

they do not contribute to localizing the objective. Moreover, due to the oscillating pattern of Bessel functions, the map of $\mathfrak{F}_{\text{BS}}(\mathbf{r}, n)$ contains several artifacts.

Property 2 (Dependency on the bistatic angle). *Since the factors $J_0(k(1 + \cos\beta)|\mathbf{r}_{obj} - \mathbf{r}|)$ and $J_0(k\sin\beta|\mathbf{r}_{obj} - \mathbf{r}|)$ that contribute to the identification are dependent on the value of β, the imaging result is considerably dependent on the bistatic angle. Therefore, the optimal number/configuration of antennas and selection of bistatic angle depend on the size and material property (contrast of permittivity/conductivity) of the objective; refer to Examples 1 and 2.*

1. *If $\beta = 0$ then since $J_0(k\sin\beta|\mathbf{r}_{obj} - \mathbf{r}|) \equiv 1$, $\Lambda_2 \equiv 0$, and $\Lambda_3 \equiv 0$,*

$$\mathfrak{F}_{BS}(\mathbf{r}, n) = J_0(2k|\mathbf{r}_{obj} - \mathbf{r}|) + \frac{2}{M} \sum_{m=1}^{M} \sum_{s=1}^{\infty} i^s J_s(2k|\mathbf{r}_{obj} - \mathbf{r}|) \cos\left(s(\theta_m - \phi_{obj})\right). \quad (9)$$

This is the generalized version of the structure derived in [28].

2. *If $\beta = \pi$, then since $J_0(k(1 + \cos\beta)|\mathbf{r}_{obj} - \mathbf{r}|) \equiv 1$ and $J_0(k\sin\beta|\mathbf{r}_{obj} - \mathbf{r}|) \equiv 1$, these terms do not contribute to determining $\mathbf{r}_{obj}$, i.e., it is impossible to recognize the objective location through the map of $\mathfrak{F}_{BS}(\mathbf{r}, n)$.*

Property 3 (Total number of measurement data). *Since $\Psi(\mathbf{r})$ can be written in the following form*

$$\Psi(\mathbf{r}) = J_0(k(1 + \cos\beta)|\mathbf{r}_{obj} - \mathbf{r}|) J_0(k\sin\beta|\mathbf{r}_{obj} - \mathbf{r}|) + \frac{1}{M} \sum_{m=1}^{M} \mathcal{E}(\mathbf{r}_{obj}),$$

where

$$\mathcal{E}(\mathbf{r}_{obj}) = (\Lambda_2 + \Lambda_3) J_0(k(1 + \cos\beta)|\mathbf{r}_{obj} - \mathbf{r}|) + \Lambda_1 J_0(k\sin\beta|\mathbf{r}_{obj} - \mathbf{r}|) + \Lambda_1(\Lambda_2 + \Lambda_3).$$

As we already examined in Property 1, the factor $\mathcal{E}(\mathbf{r}_{obj})$ disturbs the identification so that eliminating this factor is equivalent to the improvement of imaging performance. Unfortunately, we have no a priori objective information, so it is challenging to remove it. Instead, by increasing the total number M, the effect of $\mathcal{E}(\mathbf{r}_{obj})$ is negligible. This is the theoretical reason why sufficient measurement data guarantees imaging performance.

Property 4 (Antenna arrangement). *Based on the discovered structure, eliminating the terms Λ_l/M, $l = 1, 2, 3$ leads us to obtain a good result. One scenario is to increase the total number of measurement data M, but this setting seems ideal. Another possible scenario is to arrange the antenna to make $\Lambda_l = 0$ for all $l = 1, 2, 3$. Based on observation [44], if one selects the 16 uniformly distributed antennas in Figure 1, the terms Λ_l can be removed so that $\mathfrak{F}_{BS}(\mathbf{r}, n)$ defined in (4) becomes*

$$\mathfrak{F}_{BS}(\mathbf{r}, n) = J_0(k(1 + \cos\beta)|\mathbf{r}_{obj} - \mathbf{r}|) J_0(k\sin\beta|\mathbf{r}_{obj} - \mathbf{r}|).$$

4. Simulation Results

Here, we exhibit simulation results to examine the applicability and limitation of the designed imaging algorithm, and to support the theoretical result. To this end, $M = 16$ dipole antennas $\mathbf{a}_m$ were arranged uniformly on a circle of radius $R = 90\,\text{mm}$ centered at the origin such that (see Figure 1 for illustration)

$$\mathbf{a}_m = 90\,\text{mm}(\cos\theta_m, \sin\theta_m), \quad \theta_m = -90° + (m-1) \cdot 22.5°.$$

For the background material properties, we set $\varepsilon_b = 20\varepsilon_0$ and $\sigma_b = 0.2\,\text{S/m}$ at a frequency of $f = 1\,\text{GHz}$, where ε_0 denotes the vacuum permittivity. With this setting, the measurement data $\Delta S(m', m)$ and the incident field data $E_{inc}(\mathbf{a}_m, \mathbf{r})$ were generated using the CST STUDIO SUITE.

Example 1 (Imaging of a small objective). *Figure 2 shows maps of $\mathfrak{F}_{BS}(\mathbf{r}, n)$ for various n in the presence of Σ_1 with location $\mathbf{r}_1 = (10\,\text{mm}, 30\,\text{mm})$, radius $\alpha_1 = 10\,\text{mm}$, permittivity*

$\varepsilon_1 = 55\varepsilon_0$, and conductivity $\sigma_1 = 1.2\,\mathrm{S/m}$. Based on the outcome, superior imaging results were obtained when $n = 3, 4, 5, 6, 7$, i.e., $67.5° \leq \beta \leq 157.5°$, but the result was poor when $n = 1, 2$, i.e., $22.5° \leq \beta \leq 50°$ due to the appearance of several artifacts. Consequently, the sampling-type imaging is effective for identifying small objectives but the imaging performance is significantly dependent on the selection of the bistatic angle, as we discussed in Property 2. Notice that when $n = 8$, i.e., $\beta = 180°$, it is impossible to identify $\mathbf{r}_1 \in \Sigma_1$, consistent with the result in Theorem 1.
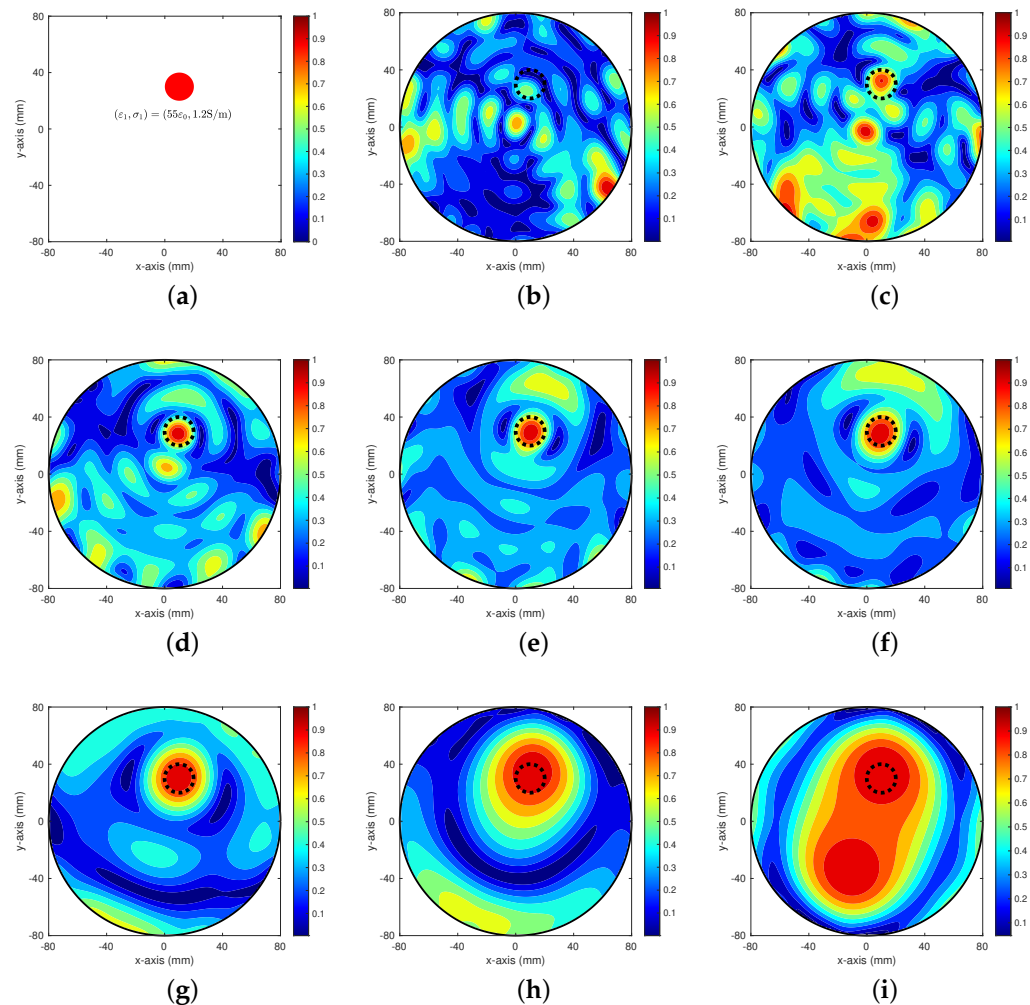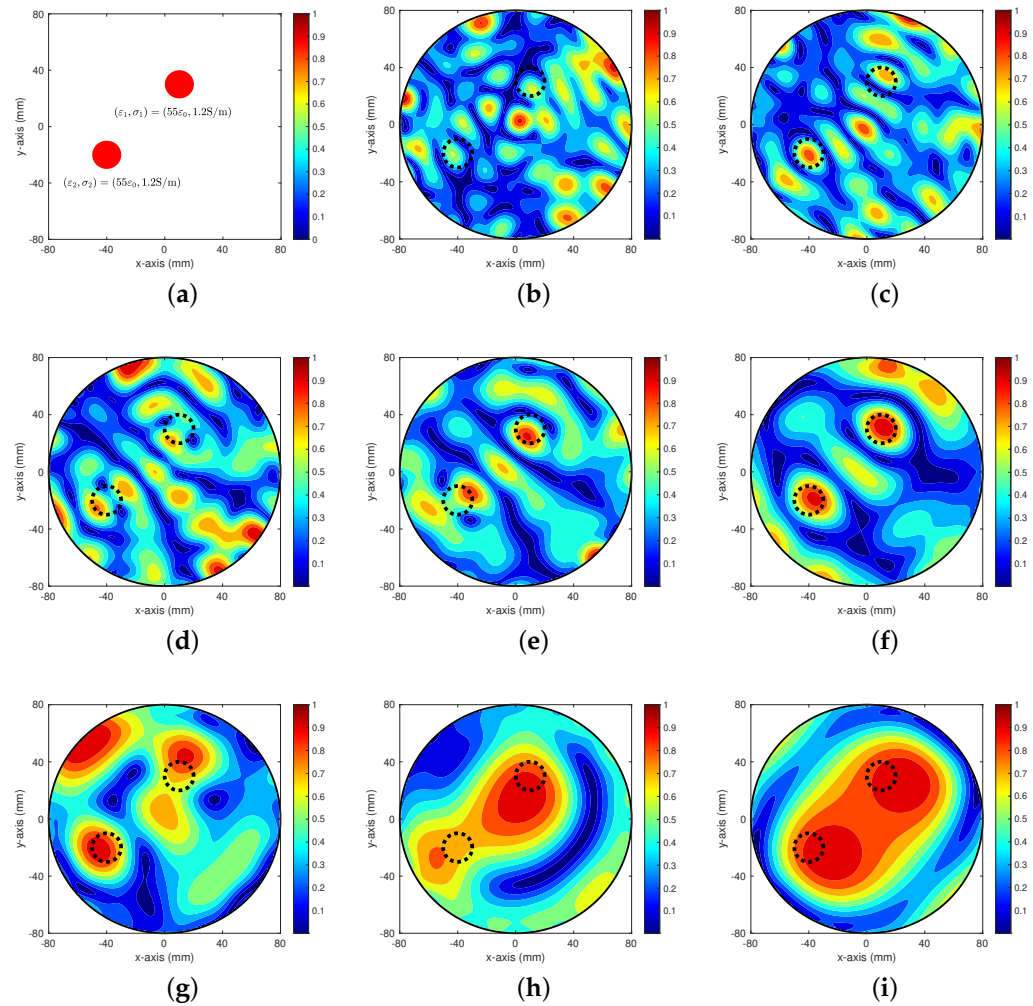

Figure 2. (Example 1) Maps of $\mathfrak{F}_{\mathrm{BS}}(\mathbf{r}, n)$. Black-colored dashed line describes the boundary of objective. (**a**) Small objective, (**b**) $n = 1$, (**c**) $n = 2$, (**d**) $n = 3$, (**e**) $n = 4$, (**f**) $n = 5$, (**g**) $n = 6$, (**h**) $n = 7$, (**i**) $n = 8$.

Example 2 (Imaging of two small objectives). *Figure 3 shows maps of $\mathfrak{F}_{\mathrm{BS}}(\mathbf{r}, n)$ for various n in the presence of Σ_1 and Σ_2. The configurations of Σ_1 are the same as in Example 1, and configurations of Σ_2 are the same as Σ_1 except the location $\mathbf{r}_2 = (-40\,\mathrm{mm}, -20\,\mathrm{mm})$. Opposite of the result in Example 1, the locations of $\mathbf{r}_1$ and $\mathbf{r}_2$ can be identified accurately only when $n = 5$, i.e., $\beta = 112.5°$. If $n = 4$ or $n = 6$, it is possible to recognize Σ_1 and Σ_2, but the identified locations are inaccurate compared to the true locations. Similar to Example 1, it is challenging to recognize the objectives when $n = 1, 2, 7$ and it is still impossible to identify them when $n = 8$.*

Figure 4 presents maps of $\mathfrak{F}_{\mathrm{BS}}(\mathbf{r}, n)$ for various n in the presence of two small objectives: Σ_1 and Σ_2. The configurations of Σ_1 and Σ_2 are the same, except for the permittivity $\varepsilon_2 = 45\varepsilon_0$ and conductivity $\sigma_2 = 1.0\,\mathrm{S/m}$. The results are very similar to the ones in Figure 3. Therefore, we can conclude that the imaging performance is significantly dependent on the selection of the bistatic angle. However, opposite to the single objective imaging, the proposed sampling algorithm must be improved for the proper identification.
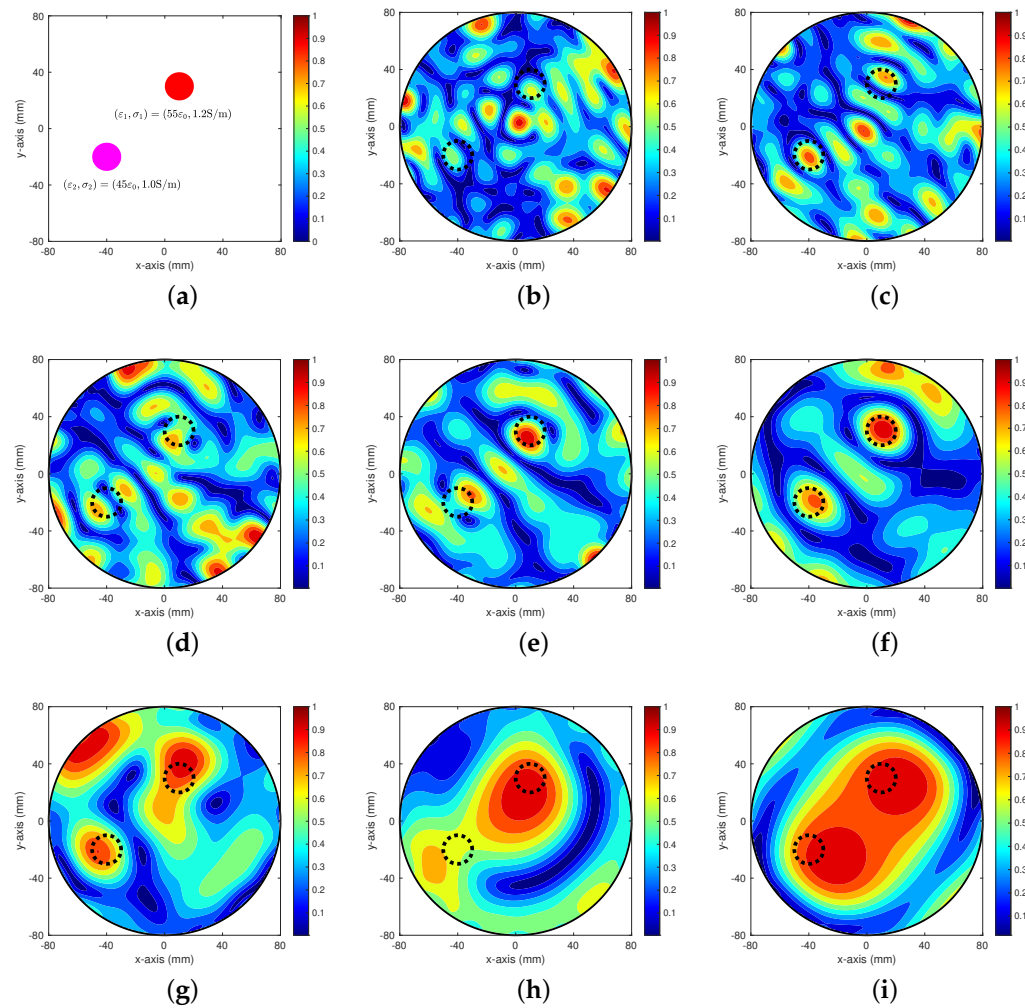
Figure 3. (Example 2) Maps of $\mathfrak{F}_{\mathrm{BS}}(\mathbf{r}, n)$. Black-colored dashed lines describe the boundaries of objectives. (**a**) Small objective, (**b**) $n = 1$, (**c**) $n = 2$, (**d**) $n = 3$, (**e**) $n = 4$, (**f**) $n = 5$, (**g**) $n = 6$, (**h**) $n = 7$, (**i**) $n = 8$.

Example 3 (Imaging of a large objective). *Here, we consider the identification of a large objective designed as a single disk circle Σ located at $\mathbf{r} = (10\,\mathrm{mm}, 20\,\mathrm{mm})$, with radius $\alpha = 50\,\mathrm{mm}$, permittivity $\varepsilon_1 = 15\varepsilon_0$, and conductivity $\sigma_1 = 0.5\,\mathrm{S/m}$. Unlike the case of small objectives, both the shape and size of the objective cannot be identified, and only the center can be recognized, refer to Figure 5. Therefore, we conclude that the designed algorithm cannot be applied directly for identifying large objectives so that the investigation of an improved imaging function is required.*

Example 4 (Imaging in the monostatic measurement configuration). *Here, we exhibit the imaging result with scattering parameter data with monostatic measurement configuration and compare the imaging performance with bistatic measurement configuration. Figure 6 shows maps of $\mathfrak{F}_{\mathrm{BS}}(\mathbf{r}, 0)$ for single (in Example 1), multiple (in Example 2), and large (in Example 3) objectives. Unlike the result in [28], the location of any objectives cannot be identified via the map of $\mathfrak{F}_{\mathrm{BS}}(\mathbf{r}, 0)$ because, as we already mentioned in Section 1, it is very difficult to extract the weak scattered signal from the relatively high antenna reflection. Hence, at this stage, we can say that direct application of the traditional monostatic imaging technique is not appropriate to identify unknown objectives.*

Figure 4. (Example 2) Maps of $\mathfrak{F}_{BS}(\mathbf{r}, n)$. Black-colored dashed lines describe the boundaries of objectives. (**a**) Small objective, (**b**) $n = 1$, (**c**) $n = 2$, (**d**) $n = 3$, (**e**) $n = 4$, (**f**) $n = 5$, (**g**) $n = 6$, (**h**) $n = 7$, (**i**) $n = 8$.

Example 5 (Imaging of a small objective with small number of measurement data)**.** *At this moment, we examine the influence of the total number of measurement data M. To this end, we exhibit simulation results for single objective Σ_1 from Example 1 with datasets $\mathcal{D}_s$, $s = 1, 2, 3$, such that*

$$\mathcal{D}_1 = \{\Delta S(1, 5), \Delta S(5, 9), \Delta S(9, 13), \Delta S(13, 1)\}$$
$$\mathcal{D}_2 = \{\Delta S(1, 5), \Delta S(4, 8), \Delta S(7, 11), \Delta S(10, 14), \Delta S(13, 1), \Delta S(16, 4)\}$$
$$\mathcal{D}_3 = \{\Delta S(1, 5), \Delta S(3, 7), \Delta S(5, 9), \cdots, \Delta S(11, 15), \Delta S(13, 1), \Delta S(15, 3)\}.$$

Based on the results in Figure 7, it is very hard to recognize the existence of Σ_1 due to the several artifacts. Therefore, to retrieve the location of Σ_1 through the $\mathfrak{F}_{BS}(\mathbf{r}, n)$, the total number M must be large enough.

Example 6 (Comparison with direct sampling method)**.** *For the final example, we apply the direct sampling method (DSM) and compare the imaging performance. Figure 8 shows the imaging results in the presence of Σ_1 from Example 1 through the DSM with location of sources $\mathbf{a}_5$, $\mathbf{a}_{10}$, and $\mathbf{a}_{15}$. Notice that the imaging performance of the DSM is significantly dependent on the location of the source and objective. However, as we have no information of the objective, selecting an optimal location of source is impossible. On the other hand, based on Example 1, the imaging performance of*

$\mathfrak{F}_{BS}(\mathbf{r}, n)$ *is dependent only on the selection of the bistatic angle, regardless of the location of the small objective.*
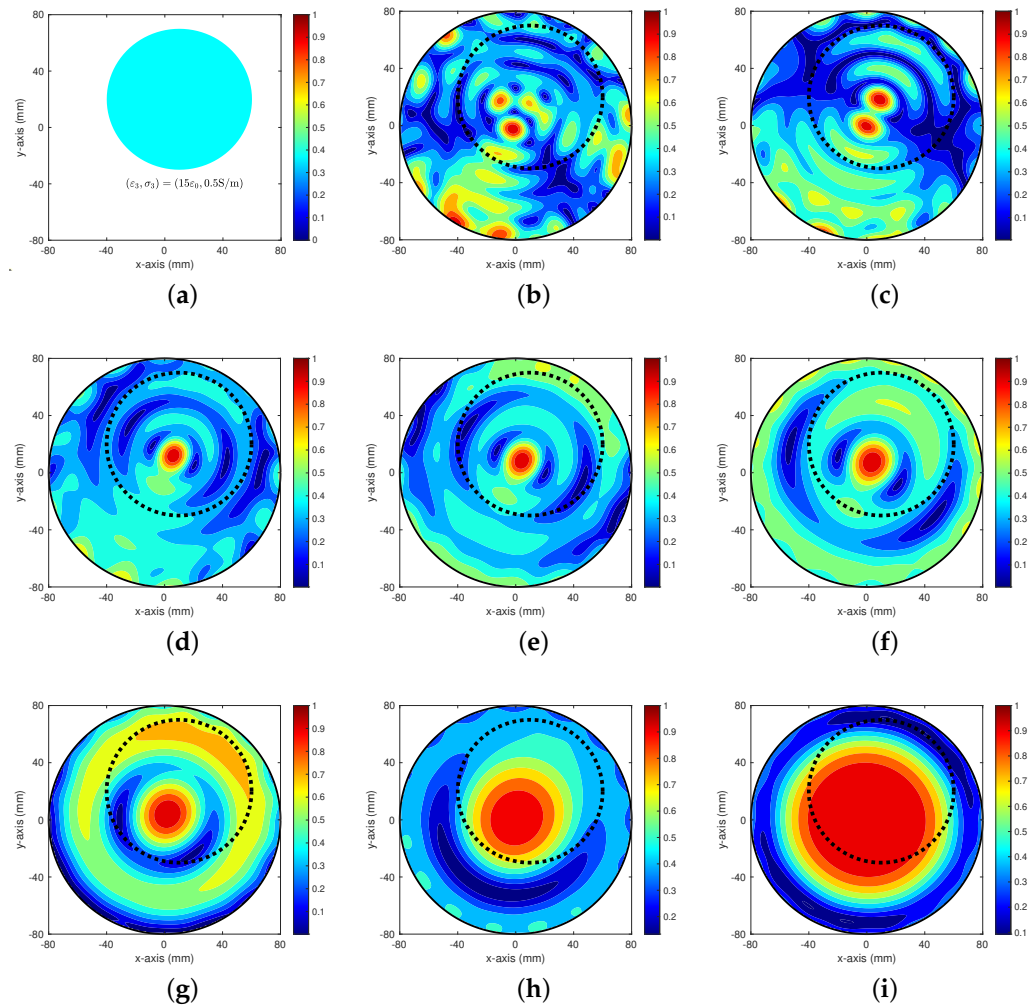

Figure 5. (Example 3) Maps of $\mathfrak{F}_{BS}(\mathbf{r}, n)$. Black-colored dashed line describes the boundary of objective. (**a**) Large objective, (**b**) $n = 1$, (**c**) $n = 2$, (**d**) $n = 3$, (**e**) $n = 4$, (**f**) $n = 5$, (**g**) $n = 6$, (**h**) $n = 7$, (**i**) $n = 8$.
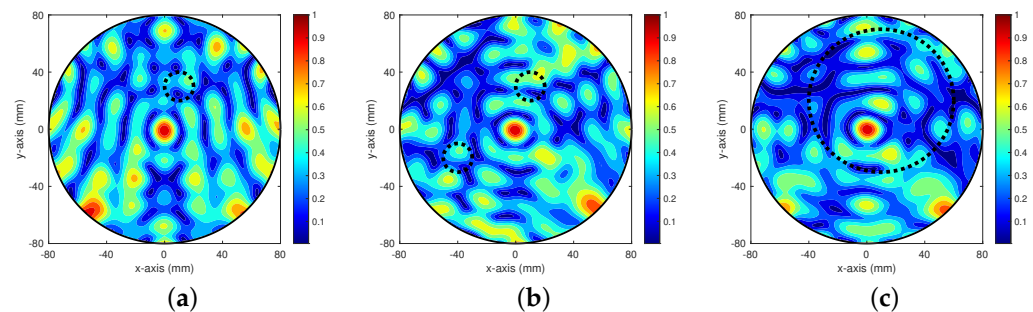
Figure 6. (Example 4) Maps of $\mathfrak{F}_{BS}(\mathbf{r}, 0)$. Black-colored dashed line describes the boundaries of objectives. (**a**) Small objective (Example 1), (**b**) Small objectives (Example 2), (**c**) Large objective (Example 3).

(a)　　　　　(b)　　　　　(c)
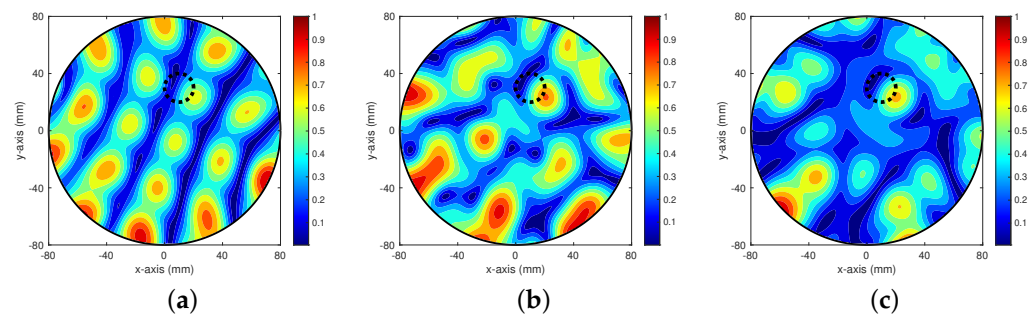
Figure 7. (Example 5) Maps of $\mathfrak{F}_{\mathrm{BS}}(\mathbf{r}, n)$ with datasets $\mathcal{D}_s$, $s = 1, 2, 3$. Black-colored dashed line describes the boundary of objective. (**a**) With dataset $\mathcal{D}_1$, (**b**) With dataset $\mathcal{D}_2$, (**c**) With dataset $\mathcal{D}_3$.

(a)　　　　　(b)　　　　　(c)
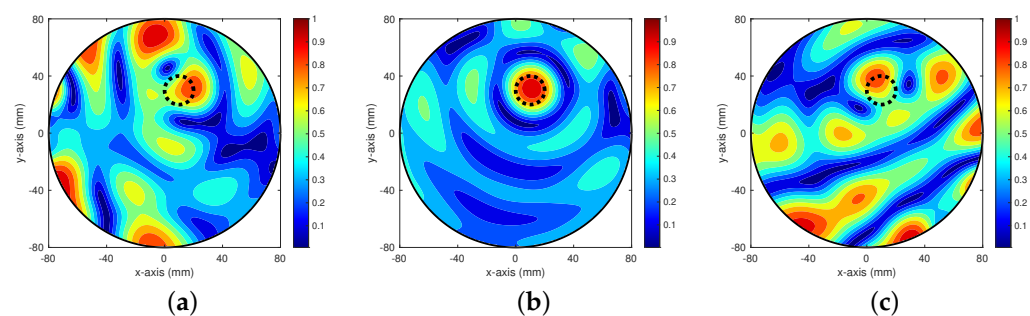
Figure 8. (Example 6) Imaging results via the direct sampling method with difference location of sources $\mathbf{a}_5$, $\mathbf{a}_{10}$, and $\mathbf{a}_{15}$. Black-colored dashed line describes the boundaries of objectives. (**a**) Imaging with source $\mathbf{a}_5$, (**b**) Imaging with source $\mathbf{a}_{10}$, (**c**) Imaging with source $\mathbf{a}_{15}$.

5. Conclusions

In this paper, a sampling-type imaging algorithm is considered for the fast identification of small objectives in the bistatic measurement configuration. Thanks to the integral equation formula for the scattered field *S*-parameter, an imaging function is designed, and its mathematical structure is proven. Based on the established structure, it is confirmed that the imaging performance is highly dependent on the bistatic angle.

Although the designed imaging technique is applicable for identifying small objectives, it is unsuitable for identifying multiple small objectives or a large objective. The enhancement of imaging performance is an interesting future research subject. Finally, there exist various millimeter wave (mmWave) imaging techniques [45,46]. We believe that investigation of an effective mmWave imaging technique in the bistatic measurement configuration will be a remarkable research topic.

Author Contributions: S.-H.S. contributed in methodology, software, validation, and writing—reviewing and editing, and funding acquisition. W.-K.P. contributed in conceptualization, methodology, software, formal analysis, investigation, writing—reviewing and editing, funding acquisition. All authors have read and agreed to the published version of the manuscript.

Conflicts of Interest: The authors declare no conflict of interest.

References

1.　Arridge, S. Optical tomography in medical imaging. *Inverse Prob.* **1999**, *15*, R41–R93.

2. Simonov, N.; Kim, B.R.; Lee, K.J.; Jeon, S.I.; Son, S.H. Advanced fast 3-D electromagnetic solver for microwave tomography imaging. *IEEE Trans. Med. Imag.* **2017**, *36*, 2160–2170.

3. Coşğun, S.; Bilgin, E.; Çayören, M. Microwave imaging of breast cancer with factorization method: SPIONs as contrast agent. *Med. Phys.* **2020**, *47*, 3113–3122.

4. Shea, J.D.; Kosmas, P.; Hagness, S.C.; Veen, B.D.V. Three-dimensional microwave imaging of realistic numerical breast phantoms via a multiple-frequency inverse scattering technique. *Med. Phys.* **2010**, *37*, 4210–4226.

5. Caorsi, S.; Massa, A.; Pastorino, M. A crack identification microwave procedure based on a genetic algorithm for nondestructive testing. *IEEE Trans. Antennas Propag.* **2001**, *49*, 1812–1820.

6. Foudazix, A.; Mirala, A.; Ghasr, M.T.; Donnell, K.M. Active microwave thermography for nondestructive evaluation of surface cracks in metal structures. *IEEE Trans. Instrum. Meas.* **2019**, *68*, 576–585.

7. Haynes, M.; Stang, J.; Moghaddam, M. Real-time microwave imaging of differential temperature for thermal therapy monitoring. *IEEE Trans. Biomed. Eng.* **2014**, *61*, 1787–1797.

8. Persson, M.; Fhager, A.; Trefnà, H.D.; Yu, Y.; McKelvey, T.; Pegenius, G.; Karlsson, J.E.; Elam, M. Microwave-based stroke diagnosis making global prehospital thrombolytic treatment possible. *IEEE Trans. Biomed. Eng.* **2014**, *61*, 2806–2817.

9. Salucci, M.; Vrba, J.; Merunka, I.; Massa, A. Real-time brain stroke detection through a learning-by-examples technique—An experimental assessment. *Microw. Opt. Technol. Lett.* **2017**, *59*, 2796–2799.

10. Mojabi, P.; LoVetri, J. Microwave biomedical imaging using the multiplicative regularized Gauss-Newton inversion. *IEEE Antennas Propag. Lett.* **2009**, *8*, 645–648.

11. Rubæk, T.; Meaney, P.M.; Meincke, P.; Paulsen, K.D. Nonlinear microwave imaging for breast-cancer screening using Gauss–Newton's method and the CGLS inversion algorithm. *IEEE Trans. Antennas Propag.* **2007**, *55*, 2320–2331.

12. Chew, W.C.; Wang, Y.M. Reconstruction of two-dimensional permittivity distribution using the distorted Born iterative method. *IEEE Trans. Med. Imag.* **1990**, *9*, 218–225.

13. Liu, Z. A new scheme based on Born iterative method for solving inverse scattering problems with noise disturbance. *IEEE Geosci. Remote Sens. Lett.* **2019**, *16*, 1021–1025.

14. Bergou, E.; Diouane, Y.; Kungurtsev, V. Convergence and complexity analysis of a Levenberg–Marquardt algorithm for inverse problems. *J. Optim. Theory Appl.* **2020**, *185*, 927–944.

15. Franchois, A.; Pichot, C. Microwave imaging-complex permittivity reconstruction with a Levenberg-Marquardt method. *IEEE Trans. Antennas Propag.* **1997**, *45*, 203–215.

16. Abubakar, A.; van den Berg, P.M.; Mallorqui, J.J. Imaging of biomedical data using a multiplicative regularized contrast source inversion method. *IEEE Trans. Microw. Theory Tech.* **2002**, *50*, 1761–1771.

17. van den Berg, P.M.; Kleinman, R.E. A contrast source inversion method. *Inverse Prob.* **1997**, *13*, 1607–1620.

18. Dorn, O.; Lesselier, D. Level set methods for inverse scattering. *Inverse Prob.* **2006**, *22*, R67–R131.

19. Irishina, N.; Dorn, O.; Moscoso, M. A level set evolution strategy in microwave imaging for early breast cancer detection. *Comput. Math. Appl.* **2008**, *56*, 607–618.

20. Park, W.K. Application of MUSIC algorithm in real-world microwave imaging of unknown anomalies from scattering matrix. *Mech. Syst. Signal Proc.* **2021**, *153*, 107501.

21. Ruvio, G.; Solimene, R.; D'Alterio, A.; Ammann, M.J.; Pierri, R. RF breast cancer detection employing a noncharacterized vivaldi antenna and a MUSIC-inspired algorithm. *Int. J. RF Microw. Comput. Aid. Eng.* **2013**, *23*, 598–609.

22. Park, W.K. Real-time microwave imaging of unknown anomalies via scattering matrix. *Mech. Syst. Signal Proc.* **2019**, *118*, 658–674.

23. Park, W.K. Real-time detection of small anomaly from limited-aperture measurements in real-world microwave imaging. *Mech. Syst. Signal Proc.* **2022**, *171*, 108937.

24. Bevacqua, M.T.; Isernia, T.; Palmeri, R.; Akinci, M.N.; Crocco, L. Physical insight unveils new imaging capabilities of orthogonality sampling method. *IEEE Trans. Antennas Propag.* **2020**, *68*, 4014–4021.

25. Son, S.H.; Lee, K.J.; Park, W.K. Application and analysis of direct sampling method in real-world microwave imaging. *Appl. Math. Lett.* **2019**, *96*, 47–53.

26. Kirsch, A. The factorization method for Maxwell's equations. *Inverse Prob.* **2004**, *20*, 117–134.

27. Chouiti, S.M.; Merad, L.; Meriah, S.M.; Derraz, F.; Raimundo, X. Monostatic imaging of an embedded object using a confocal algorithm. *Int. J. Numer. Model.* **2018**, *31*, 1–14.

28. Kang, S.; Lambert, M.; Park, W.K. Analysis and improvement of direct sampling method in the mono-static configuration. *IEEE Geosci. Remote Sens. Lett.* **2019**, *16*, 1721–1725.

29. Zetik, R.; Thoma, R.S. Monostatic imaging of small objects in UWB sensor networks. In Proceedings of the 2008 IEEE International Conference on Ultra-Wideband, Hannover, Germany, 10–12 September 2008; Volume 2, pp. 191–194.

30. Son, S.H.; Simonov, N.; Kim, H.J.; Lee, J.M.; Jeon, S.I. Preclinical prototype development of a microwave tomography system for breast cancer detection. *ETRI J.* **2010**, *32*, 901–910.

31. Park, W.K. Theoretical identification of coupling effect and performance analysis of single-source direct sampling method. *Mathematics* **2021**, *9*, 1065.

32. Chernyak, V.S. *Fundamentals of Multisite Radar Systems: Multistatic Radars and Multiradar Systems*; CRC Press: Boca Raton, FL, USA, 1998.

33. Sasada, S.; Masumoto, N.; Song, H.; Emi, A.; Kadoya, T.; Arihiro, K.; Kikkawa, T.; Okada, M. Microwave breast imaging using rotational bistatic impulse radar for the detection of breast cancer: Protocol for a prospective diagnostic study. *JMIR Res. Protoc.* **2020**, *9*, e17524.

34. Lin, D.B.; Chu, T.H. Bistatic frequency-swept microwave imaging: Principle, methodology and experimental results. *IEEE Trans. Microw. Theory Tech.* **1993**, *41*, 855–861.

35. Comblet, F.; Khenchaf, A.; Baussard, A.; Pellen, F. Bistatic synthetic aperture radar imaging: Theory, simulations, and validations. *IEEE Trans. Antennas Propag.* **2006**, *54*, 3529–3540.

36. Welsh, B.M.; Gardner, C.S. Bistatic imaging lidar technique for upper atmospheric studies. *Appl. Opt.* **1989**, *28*, 82–88.

37. Liang, B.; Shang, X.; Zhuge, X.; Miao, J. Bistatic cylindrical millimeter-wave imaging for accurate reconstruction of high-contrast concave objects. *Opt. Express* **2019**, *27*, 14881–14892.

38. Cherniakov, M. *Bistatic Radar: Principles and Practice*; Wiley: Hoboken, NJ, USA, 2007.

39. Griffiths, H.D. Bistatic and multistatic radar. In Proceedings of the Institution of Electrical Engineers Military Radar Seminar, Shrivenham, UK, 28–30 October 2004.

40. Kang, S.; Lim, M.; Park, W.K. Fast identification of short, linear perfectly conducting cracks in the bistatic measurement configuration. *J. Comput. Phys.* **2022**, *468*, 111479.

41. Willis, N.J.; Griffiths, H.D. *Advances in Bistatic Radar*; The Institution of Engineering and Technology: London, UK, 2007.

42. Slaney, M.; Kak, A.C.; Larsen, L.E. Limitations of imaging with first-order diffraction tomography. *IEEE Trans. Microw. Theory Tech.* **1984**, *32*, 860–874.

43. Colton, D.; Kress, R. *Inverse Acoustic and Electromagnetic Scattering Problems*; Mathematics and Applications Series; Springer: New York, NY, USA, 1998.

44. Kang, S.; Chae, S.; Park, W.K. A study on the orthogonality sampling method corresponding to the observation directions configuration. *Res. Phys.* **2022**, *33*, 105108.

45. Wang, C.; Qin, C.; Yao, Y.; Li, Y.; Wang, W. Low complexity interference alignment for mmWave MIMO channels in three-cell mobile network. *IEEE J. Sel. Areas Commun.* **2017**, *35*, 1513–1523.

46. Xu, W.; Gao, F.; Zhang, J.; Tao, X.; Alkhateeb, A. Deep learning based channel covariance matrix estimation with user location and scene images. *IEEE Trans. Commun.* **2021**, *69*, 8145–8158.